ACS APPLIED MATERIALS & INTERFACES

Research Article

www.acsami.org

Facile Synthesis of Optical Microcavities by a Rationally Designed Anodization Approach: Tailoring Photonic Signals by Nanopore Structure

Ye Wang,[†,‡] Yuting Chen,[†] Tushar Kumeria,[†] Fuyuan Ding,[†] Andreas Evdokiou,*[,‡] Dusan Losic,*[,†] and Abel Santos*[,†]

[†]School of Chemical Engineering, The University of Adelaide, Adelaide, SA 5005, Australia

[‡]Discipline of Surgery, Basil Hetzel Institute, The University of Adelaide, Adelaide, SA 5005, Australia

Supporting Information

ABSTRACT: Structural engineering of porous anodic aluminum oxide (AAO) nanostructures by anodization has been extensively studied in the past two decades. However, the transition of this technique into the fabrication of AAO-based one-dimensional photonic crystal is still challenging. Herein, we report for the first time on the fabrication of AAO optical microcavities by a rationally designed anodization approach. In our study, two feasible methods are used to fabricate microcavities with tunable resonance peak across the visible and near-infrared spectra. Distributed Bragg reflector (DBR) nanostructures are first fabricated by pulse anodization approach, in which the anodization voltage was periodically manipulated to achieve pseudosinusoidal modulation of the effective refractive index gradient along the depth of the AAO nanostructures. Microcavities were created by creating a nanoporous layer of constant porosity between two AAO−DBR nanostructures, and by introducing a shift of the phase of the porosity gradient along the depth of AAO. The position of the resonance peak in these microcavities can be linearly tuned by means of the duration of the high voltage anodization. These optical nanostructures are sensitive to alterations of the effective media inside the nanopores. The AAO microcavity shows a central wavelength shift of 2.58 ± 0.37 nm when exposed to water vapor. Our research highlights the feasibility of anodization technique to fabricate AAO-based photonic nanostructures for advanced sensing applications.

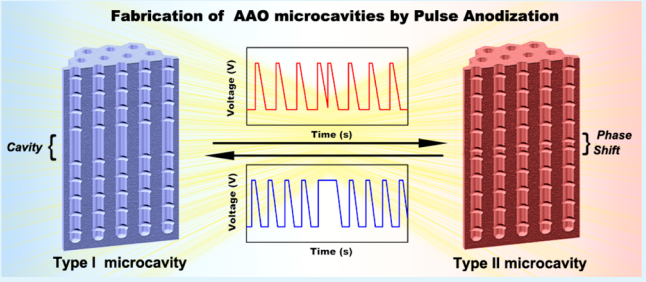

KEYWORDS: *electrochemical anodization, anodic aluminum oxide, nanopores, photonic crystal, distributed Bragg reflectors, microcavities, chemical sensing*

INTRODUCTION

Intensive and extensive research studies on nanoporous anodic aluminum oxide (AAO) prepared by self-ordering electrochemical anodization have stimulated numerous advanced applications in recent decades such as nanofabrication, optical sensing, energy storage, and drug delivery.[1−4] In particular, AAO has gained considerable interests in recent years for chemical sensing and biosensing mainly due to its scalable and cost-competitive fabrication process, high surface area, excellent chemical and mechanical stability, and tunable pore geometry.[5] High aspect ratio AAO nanostructures with straight cylindrical geometry are conventionally fabricated by a technique of so-called mild anodization (MA) with regard to the slow growth rate of the oxide film (2−7 μm/h) under low current density (j = 1−5 mA/cm^2).[6] Experimental studies and theoretical models have confirmed that the formation of self-organized nanoporous anodic films is due to the mechanical stress driven by the migration of ions (i.e., Al^{3+} and O^{2-}) across the oxide barrier layer as well as field-enhanced dissolution of oxide.[7−11] Since the mechanical stress and electrochemical oxidation rate are proportional to the ionic current passing through the oxide layer, the current density applied during anodization governs the growth rate of the anodic oxide and also the geometric features of the resulting nanoporous film such as the nanopore's size and its shape.[10] For example, AAO with high growth rates and large pore diameters can be produced when the anodization process is carried out under high current densities (j > 30 mA/cm^2).[12] Importantly, the elucidation of the formation mechanism of AAO has recently boosted numerous studies on the fabrication of novel AAO-based photonic nanostructures. AAO structures based on stacks of periodic dielectric nanoporous layers with sinusoidally patterned effective refractive index display tunable photonic stop bands (i.e., wavelength ranges where the material present high reflectivity and low/limited transmittance of light).[13] In contrast to straight nanopores, AAO with modulated or

Received: March 2, 2015
Accepted: April 22, 2015
Published: April 22, 2015

DOI: 10.1021/acsami.5b01885
ACS Appl. Mater. Interfaces 2015, 7, 9879−9888

Scheme 1. Illustration of Fabrication Process of AAO Microcavities by Pulse Anodization[a]

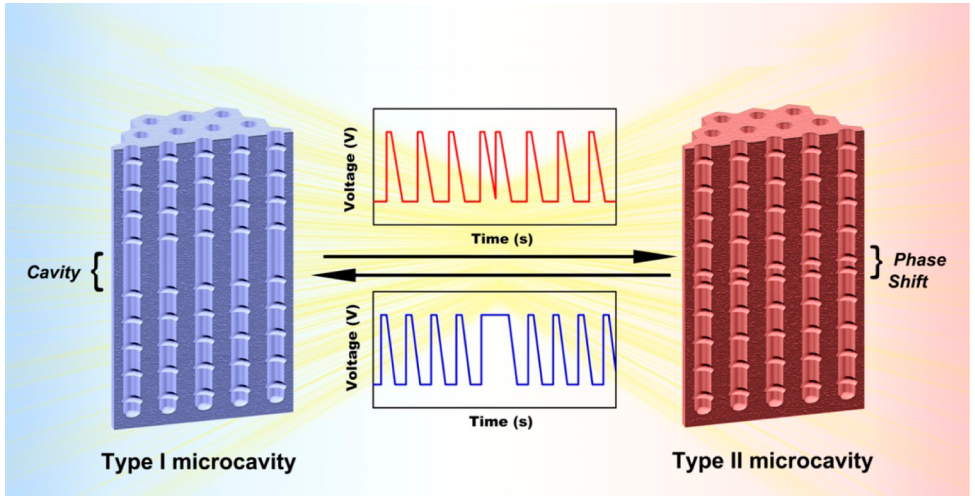

[a]Type I microcavities are prepared by inserting a cavity layer between two AAO−DBR structures (left side). Type II microcavities are fabricated by shifting the phase of anodization profile to achieve the phase modulation of effective refractive index in the bottom DBR structures (right side).

hierarchically branched nanopores can be fabricated by continuous periodic manipulation of the current density/voltage during anodization. This electrochemical approach, so-called pulse anodization,[14−18] makes it possible to precisely tailor the effective refractive index profile of AAO in depth in order to generate distributed Bragg reflectors (DBR).[19−23] Several recent studies have demonstrated the potential of AAO-based DBR nanostructures for chemical and biological sensing applications.[24−26]

The understanding of the anodization mechanism has tremendously enhanced our ability to fabricate AAO featuring sophisticated nanostructures. However, more extensive fundamental research must be carried out in order to develop novel AAO-based photonic structures with optimized optical properties. In this scenario, here we report on a rationally designed synthesis approach aimed to fabricate AAO-based optical microcavities for potential chemical vapor sensing. AAO microcavities are prepared by pulse anodization, in which the nanostructure of AAO is directly manipulated by the anodization voltage in order to modulate the effective refractive index of the nanoporous structure in depth. The AAO microcavities, similar to other thin-film microcavities,[27−30] are formed by inserting a thin layer of nanopores with constant effective refractive index between two highly reflective DBR structures (type I microcavities) as well as by shifting the phase of the refractive index along the depth of AAO (type II microcavities) (Scheme 1). We demonstrate that both strategies are feasible solutions for fabricating AAO microcavities with tunable position of the resonance peak. The sensing capabilities of the AAO microcavities are tested by using water vapor as a model gas. Our result provides promising opportunities for preparing more sophisticated AAO-based photonic nanostructures for advanced applications, such as optical interference filters, light harvesting devices, and environmental sensors.

EXPERIMENTAL SECTION

Materials and Chemicals. Aluminum (Al) foils of thickness 0.32 mm and purity 99.9997% were supplied by Goodfellow Cambridge Ltd. (Wrexham, U.K.). Oxalic acid ($H_2C_2O_4$), copper(II) chloride ($CuCl_2$), hydrochloric acid (HCl), ethanol (denatured; C_2H_5OH), perchloric acid ($HClO_4$), chromium trioxide (CrO_3), and phosphoric acid (H_3PO_4) were purchased from Sigma-Aldrich (Castle Hill, Australia) and used without further processing. Ultrapure water Option Q-Purelabs (Castle Hill, Australia) was used for preparing all of the solutions used in this study.

Table 1. Summary of Anodization Conditions Used to Fabricate the Two Types of Microcavities Produced in This Study

	type I microcavities		type II microcavities	
serial no.	HVA duration (s)	cavity anodization duration (min)	phase change	HVA duration (s)
1	140	20	1/2 π	140
2	180	20	π	140
3	240	10−20	3/2 π	140
4	300	20	7/4 π	140
5	360	20		

Fabrication of AAO Microcavities by Pulse Anodization. The AAO microcavities were synthesized by a modified pulse anodization process.[21,31] Briefly, Al chips 1.5 cm in diameter were first sonicated in ethanol and ultrapure water. Al chips were electropolished prior to anodization in a mixture of ethanol and $HClO_4$ 4:1 (v:v) at 20 V and 5 °C for 3 min. After this, the first anodization step was carried out in an electrolyte of 0.3 M $H_2C_2O_4$ at 40 V and 6 °C for 20 h. The resulting AAO layer was dissolved by wet chemical etching in a solution of 0.2 M chromic acid (H_2CrO_4) and 0.4 M H_3PO_4 at 70 °C for 3 h. Subsequently, pulse anodization was conducted at 5 °C with vigorous stirring. A Keithley 2400 source-meter unit was used to control the pulse parameters. The area exposed to the electrolyte solution was 0.95 cm^2, and the current density (j) was calculated by dividing the input current by the anodized sample area. In general, a pulse cycle contains three steps: (1) a constant high voltage step, named high voltage anodization (HVA), was first conducted at 50 V for a certain period of time, which ranged from 140 to 360 s. (2) Then the voltage was gradually reduced to 20 V at a rate of 0.078 V/s. (3) Finally, the anodization voltage was kept at 20 V, stage named low voltage anodization (LVA), for 8 min. A typical AAO−DBR nanostructure was first fabricated by applying 40 pulse cycles of anodization following the aforementioned protocol. To fabricate AAO microcavities with cavity layers (type I microcavities), an AAO−DBR structure was first created by 20 pulse anodization cycles. Then, the anodization process was continued at 50 V under a designed duration to achieve an optimum thickness of the cavity layer. This was followed by another set of 20

DOI: 10.1021/acsami.5b01885
ACS Appl. Mater. Interfaces 2015, 7, 9879−9888

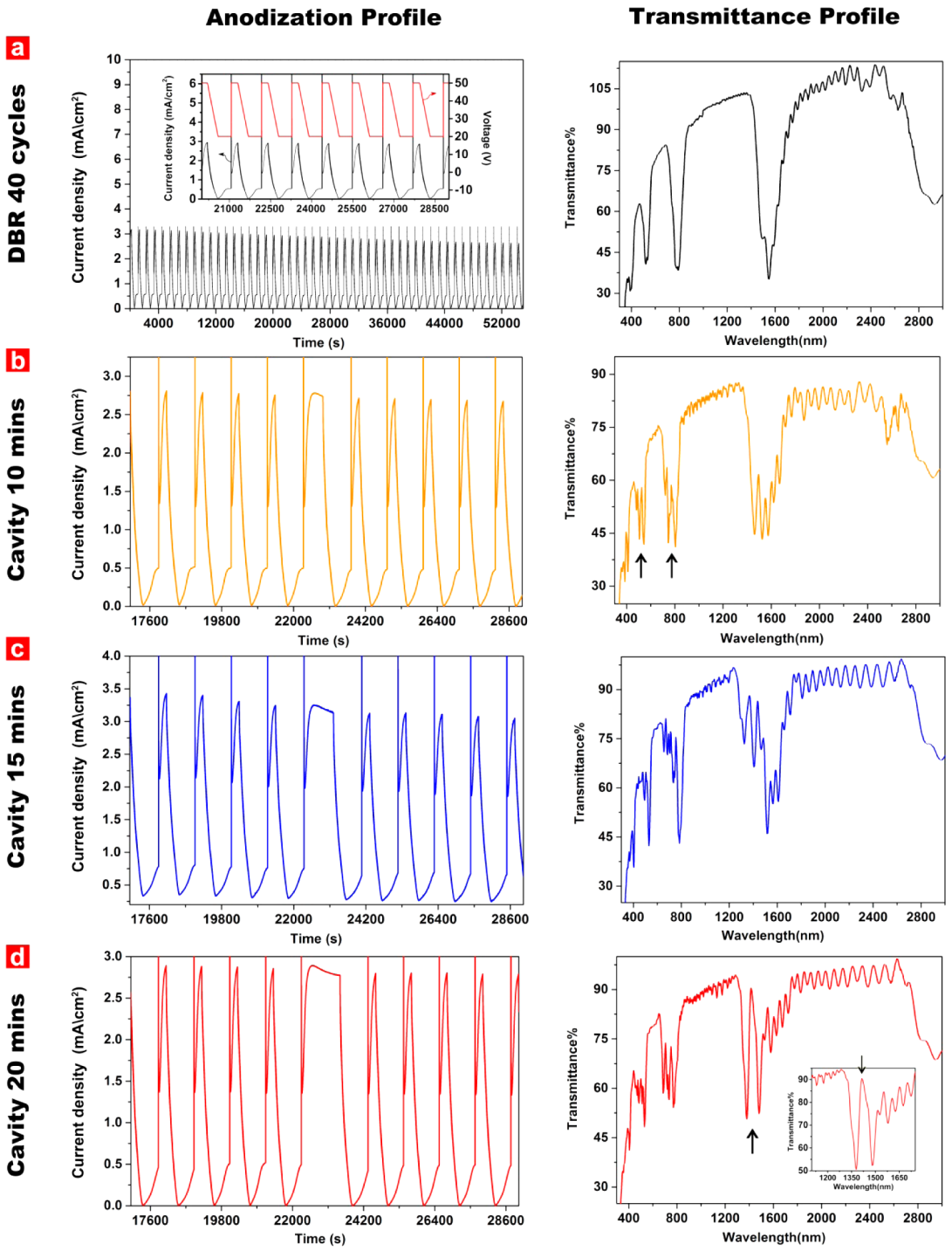

Figure 1. Anodization profiles and transmittance spectra of AAO−DBR and AAO microcavities (type I). (a) AAO−DBR is prepared by 40 cycles' pulse anodization. Each pulse cycle consisted of a 240 s anodization at 50 V, a programmed reduction of voltage to 20 V at the rate of 0.078 V/s, and a 480 s anodization at 20 V. Inset represents an enlarged anodization profile. (b−d) Optimization of cavity layer thickness for preparing microcavities. The cavity layer was sandwiched between two DBR nanostructures anodized continuously with 20 cycles' pulse, respectively. The cavity layer thickness was controlled by anodization at 50 V for (b) 10, (c) 15 min and (d) 20 min, respectively. Black arrows denote the positions of the resonance peaks of microcavities.

cycles of pulse anodization to form another AAO−DBR structure at the bottom of the resulting AAO film (Scheme 1, left side). The synthesis conditions of type II AAO microcavities are the same as those used to produce microcavities of type I (i.e., 5 °C; HVA of 140 s/50 V; LVA of 480 s/20 V; and 40 pulse cycles in total) except that a phase change is introduced at the 20th pulse cycle instead of growing cavity layers (Scheme 1, right side). For instance, after fabrication of the first DBR structure, the pulse phase was shifted 1/2 π at the 20th pulse. Then, the process was continued with a series of 20 pulses at 1/2 π phase shift. This process makes it possible to create an optical microcavity (i.e., optical interface) between the two DBR structures without any physical layer between both DBRs. Once the anodization process was finished, the remaining aluminum substrate was selectively removed from the backside of these Al chips by wet chemical etching through an etching mask in a saturated solution of $HCl/CuCl_2$. A pore-widening process was performed by wet chemical etching in

DOI: 10.1021/acsami.5b01885
ACS Appl. Mater. Interfaces 2015, 7, 9879−9888

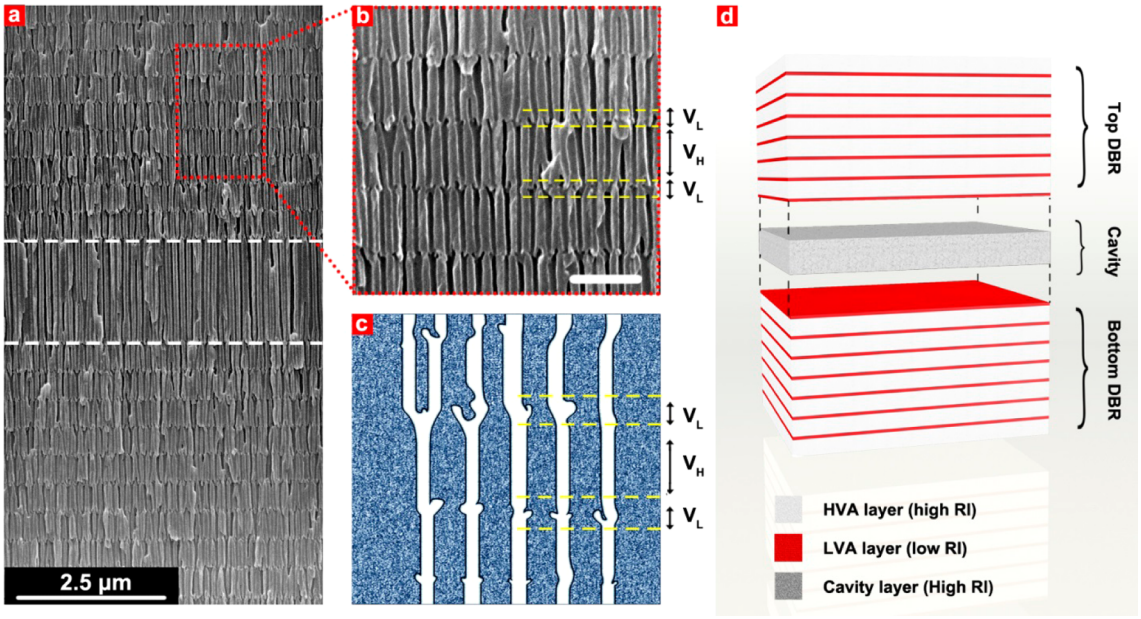

Figure 2. Structural characterization of AAO microcavities (type I). (a) SEM cross-section image of the AAO microcavities with cavity layer thickness of 1.770 ± 0.014 μm after 20 min anodization at 50 V. White dashed line denotes the boundary of the cavity layer. (b) Magnified view of the DBR layer indicated in panel a by a red rectangle. The yellow dashed line denotes the boundaries of the high voltage anodization (HVA) layer and low voltage anodization (LVA) layer. V_L is low voltage, while V_H denotes high voltage. Scale bar: 500 nm. (c) Schematic illustration of the nanopore structure, which contains straight pores in the HVA layer and a branched structure at the LVA layer. (d) Scheme of the structure of AAO microcavities (type I) containing a cavity layer sandwiched between two DBR layers. The modulation of refractive index (RI) is achieved by alternating HVA and LVA layers in a sequential manner.

freshly prepared H_3PO_4 solution at a concentration of 5 wt % at 35.0 ± 0.1 °C for 12 min. The fabrication conditions used to produce the previously mentioned microcavities are summarized in Table 1.

Structural Characterizations. The structural characteristics of the AAO microcavities were established from SEM images acquired by a field emission gun scanning electron microscope (FEG-SEM FEI Quanta 450). The transmission spectra were obtained by using UV−vis−near-IR spectroscopy (Cary 5000, Agilent). The spectra were collected from 300 to 3000 nm at a resolution of 5 nm. To conduct the Lorentzian fit of the resonance peak, the spectra resolution was adjusted to 0.1 nm. The optical images of AAO microcavities were captured by a digital camera (Nikon D3100).

Water Vapor Sensing. To test the sensitivity of AAO microcavities to chemical vapors, 3 mL of ultrapure water was added in a 5 mL hydrothermal autoclave reactor and preheated to 70 °C. Since this process was conducted in such conditions that water vapor was in thermodynamic equilibrium with its condensed state, the vapor pressure as a function of temperature can be determined by the Clausius−Clapeyron relation, which is estimated to be 31.1760 KPa at 70 °C. Type II AAO microcavities prepared by a 7/4 π phase shift was placed on the top of the reactor and faced down to allow the infiltration of vapor into its nanopores. After certain accumulated time course (i.e 10, 30, 60, 120, and 240 s), the sample was assessed immediately by UV−vis−near-IR spectroscopy at the wavelength range from 850 to 1100 nm with a resolution of 1 nm.

Unless otherwise indicated, all of the aforementioned experiments were repeated three times, and the obtained values of the different characteristic parameters were statistically treated by calculating averages and standard deviations.

RESULTS AND DISCUSSION

Synthesis of AAO Microcavities (Type I) by Optimizing the Thickness of the Cavity Layer. For a DBR structure containing dielectric stacks with alternated effective refractive indexes, the optical thickness of each stack should be equal to a quarter of the wavelength at which the light reflection is maximum in order to achieve constructive interference of light according to the Bragg condition,

$$n_H d_H = \lambda/4 = n_L d_L \quad (1)$$

where n_H/d_H and n_L/d_L are the effective refractive indices and thicknesses of the corresponding layers with high and low effective refractive index, respectively.[27,32,33] To create a narrow resonance (microcavity) in the stop band of a DBR, a cavity layer with half-wavelength optical thickness is inserted in the middle of the dielectric stacks. This makes it possible to create destructive interferences at a certain wavelength, which is established by the characteristics of the cavity layer. Therefore, the design of thin-film optical microcavities requires a precise control over the thickness and effective refractive index of each layer on the DBR and the cavity layer, since very slight deviations of these structures will lower the quality of the optical cavity. Note that long-term aluminum anodization (>24 h) unavoidably decreased the electrolyte concentration and consequently reduced the current density, which makes the quality control of each stack layer a challenge.[34]

AAO microcavities (type I) with a physical cavity layer sandwiched in between two AAO-DBR structures were produced by pulse anodization of aluminum (Figure 1). Figure 1a shows the anodization profile and transmittance spectrum of an AAO−DBR pulse anodized by 40 cycles. To achieve the variation of effective refractive index, the voltage was engineered from 50 to 20 V in a periodic fashion. Note that direct switching voltage from 50 to 20 V blocks the growth of nanopore due to the delayed current recovery caused by the thick oxide barrier layer formed during previous HVA. In a given electrolyte, the barrier layer thickness increases with the anodization potential (U) with a proportional rate of 1.3 nm V^{-1} for MA process.[12] However, at voltage control condition,

DOI: 10.1021/acsami.5b01885
ACS Appl. Mater. Interfaces 2015, 7, 9879−9888

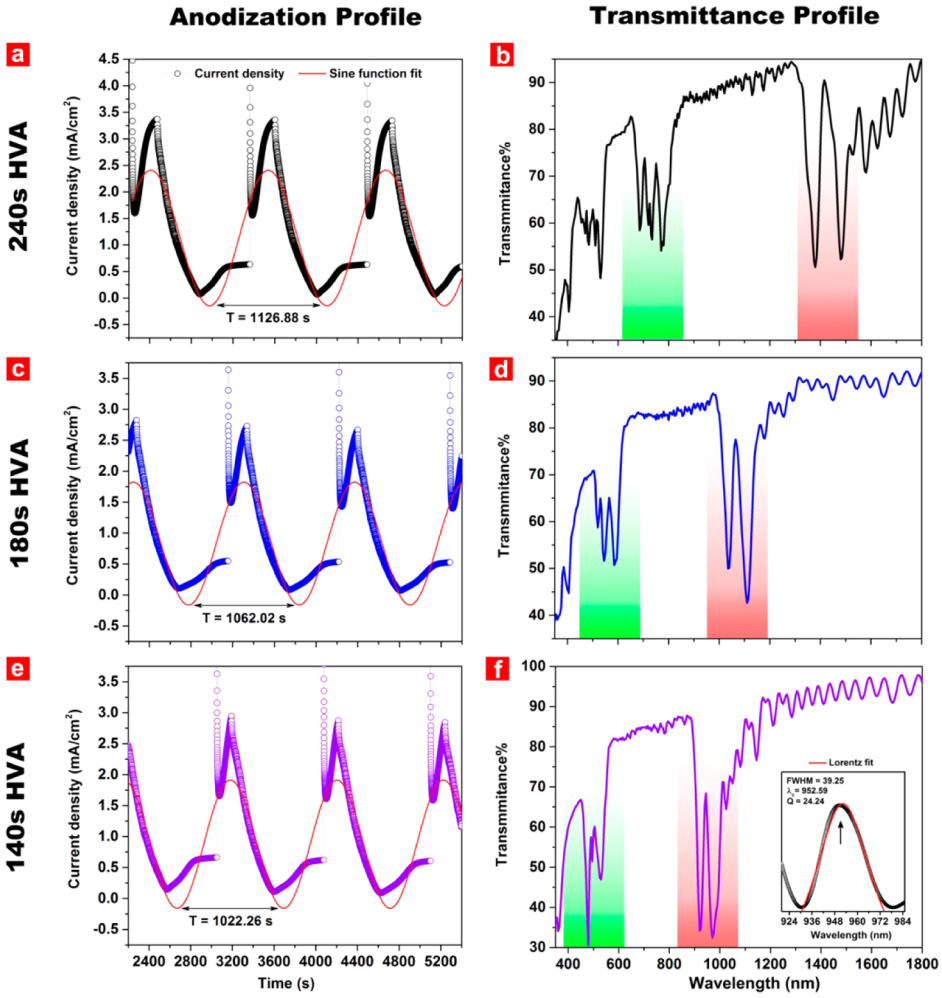

Figure 3. Manipulation of the AAO microcavities stop band position by changing high voltage anodization (HVA) duration. (a, c, e) Current density−time profile of pulse anodization with HVA duration of 240, 180, and 140 s, respectively. Sine function fitting was applied as an illustration of pseudosinusoidal current density profile. (b, d, f) Transmittance profiles of the resulting AAO microcavities prepared under different HVA durations. Red color region denotes the position of the first order stop band. Green region denotes the position of the second order stop band. The blue shift of stop band is evident when the HVA duration is decreased. Inset is a magnification of the cavity resonance of AAO microcavities prepared by 140 s HVA. Lorentz fit was applied, and the quality factor of these AAO microcavities was determined to be 24.24.

the current density is inversely proportional to the logarithm of the barrier layer thickness according to the high field conduction theory,

$$j = j_0 \exp(\beta \Delta U / t_b) \quad (2)$$

where j is current density, j_0 and β are material-dependent constants at a given temperature, and $\Delta U/t_b$ is the effective electric field strength across the barrier thickness, t_b.[2] From this expression we can infer that when the voltage is reduced from high to low with a large potential difference, the thickness of the barrier layer remains at a thick level, while the effective field strength at LVA is not strong enough to keep the ionic flow (i.e., Al^{3+} and O^{2-}) through the thick oxide barrier layer at the pore bottom tips. To overcome this limitation, a decreasing voltage ramp was applied at a rate of 0.078 V/s, which is the fastest possible according to our results. After 12 min of pore widening treatment, the porosity contrast between layers increases, and the transmittance spectra of the AAO−DBR presents three characteristic resonance peaks at the wavelengths of 1550, 790, and 520 nm. To create a microcavity resonance peak, a cavity layer was fabricated by HVA at designed duration (i.e., 10, 15, and 20 min) as shown in Figure 1b−d. The resulting transmittance spectra clearly showed the evolution of the resonance peaks with regard to the thickness of the cavity layer, in which the first order resonance peak at the wavelength of 1415 nm was formed completely with a HVA cavity layer of 20 min. SEM characterization revealed that the thickness of the cavity layer after 20 min of HVA was 1.770 ± 0.014 μm (Figure 2a). Figure 2b shows a magnified view of the DBR structure. It is evident that straight pores were formed at the HVA section while branching structure appeared during LVA. Previous studies on pore branching phenomenon in AAO showed that the number of branched nanopores can be precisely engineered by reducing the voltage by a factor of $1/\sqrt{n}$, where n is the number of branches per pore.[39−41]

Note that this condition cannot be accomplished unless a chemical etching step is performed to reduce the oxide barrier layer thickness and allow the flow of ions (i.e., Al^{3+} and O^{2-}) at reduced voltage. In our protocol, the potential was reduced approximately by a factor of $1/\sqrt{6}$. However, we only observed two-branch structure in a competitive growth pattern (Figure 2b,c and Supporting Informaton (SI) Figure S1). This phenomenon is thought to be associated with the uneven distribution of the electric field at the bottom of nanopores due

DOI: 10.1021/acsami.5b01885
ACS Appl. Mater. Interfaces 2015, 7, 9879−9888

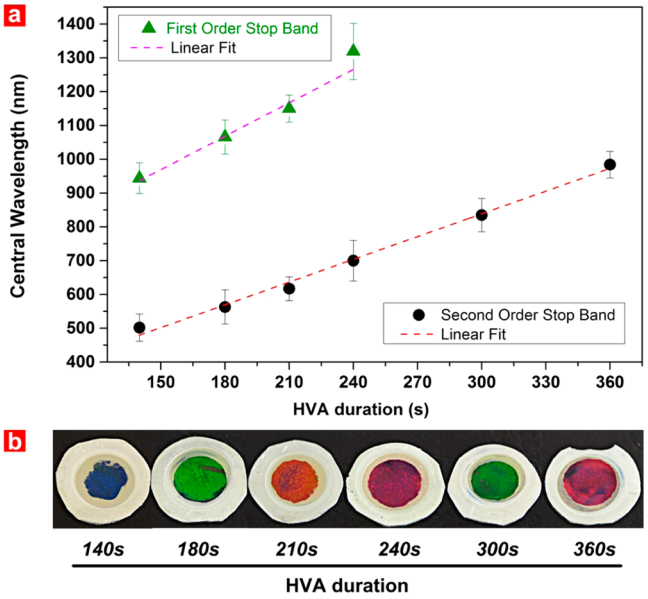

Figure 4. Relation of central wavelength position and resulting color of AAO microcavities against high voltage anodization duration. (a) Linear fitting of central wavelength position against the HVA duration. The first and second order stop band positions can be tailored across the range of visible and near-infrared wavelength. (b) The color of AAO microcavities can be precisely controlled by HVA duration.

to the continuous reduction of voltage.[36] Interestingly, the branching nanopores did not grow steadily but formed as tips at the interfaces of HVA and LVA layers. This phenomenon is due to the unregulated growth of nanopore at the disordered growth regime. In the condition of LVA, the anodization was conducted at 20 V/0.3 M oxalic acid, which is far from the self-organized regime in oxalic acid (40 V).[9] In addition, although the duration of LVA was twice longer than HVA, the growth rate of nanopore was slow due to the delayed current recovery as well as reduced ion current density according to eq 2. Therefore, such undeveloped branching pores increased the porosity in the LVA layer, thus leading to low effective refractive index. In contrast, HVA led to a relatively lower porosity, which generates higher effective refractive index as compared to LVA (Figure 2d). Accordingly, the programmed anodization profile creates a periodically modulated porosity, which in turn results in a DBR structure.[35,36] This engineered periodical porosity pattern enabled the accumulation of in phase interference from each dielectric stack, thus achieving the sharp characteristic reflection peak of the DBR as shown in Figure 1a. Since pulse anodization is frequently used to produce AAO-based photonic nanostructures, clarifying the mechanism of porous growth pattern during voltage shifting is of fundamental importance for controlling the porosity of dielectric stacks. Another advantage of this fabrication approach is that the performance of microcavities is mainly determined by the thickness of the cavity layer as illustrated in Figure 2d. Therefore, one can precisely design the cavity structure by HVA, in which the growth rate of pores is linear with the duration of anodization.

Tuning Resonance Peak Position by Engineering HVA Duration. From SEM structural characterization, the layer thickness of the HVA layer is considerably thicker than that of the LVA layer. We reasoned that tuning the HVA layer thickness may affect the stop band position of the DBR, as the stop band wavelength is proportional to the effective media of dielectric stacks according to eq 1. As shown in Figure 3, reducing HVA duration from 240 to 140 s without changing the cavity structure readily shifted the position of the first order resonance peak from 1415 to 945 nm. The resonance wavelength value of the sample of 140 s HVA was determined by fitting a Lorentzian curve to the experimental data, which had a quality factor of 24.24 with full width at half-maximum (FWHM) of 39.25 nm (Figure 3f). Note that the current density profile in our condition can be treated as a pseudosinusoidal profile when fitted to a sine function (Figure 3a,c,e). As we discussed earlier, the anodization voltage influences the barrier layer thickness, while it is the ionic current density that dominates the geometry of the nanopore such as nanopore diameter and branching feature. It is known that the nanopore geometry is influenced by the mechanical stress over the barrier layer, which is governed by the ionic current density passed through the barrier layer at a given potential according to eq 2.[10,42] When the potential drops from a high to a low value, the concurrently reduced current density will decrease the compressive stress over the barrier layer due to retarded ionic migration moved from cell bottom toward cell boundary, which leads to the uneven distribution of current density at the bottom, and consequently result in the modulation of nanopore geometry and branching structure.[7,8] Therefore, the periodical current density pattern engineered the effective refractive index profile into a pseudosinusoidal pattern, which makes it possible to manipulate the photonic stop band position by changing the anodization period.[37,38,43]

This strategy enables us for the first time to control the resonance peak of AAO microcavities and tune its position across the visible and near-infrared spectra. The positions of the resonance peak are linear with the duration of HVA (Figure 4). The visual color of these photonic structures is dominated by the second order stop band when HVA is below 240 s, while the third order of the stop band starts to induce color when the HVA is higher than 300 s. Note that the features of cavities (i.e., thickness and effective refractive indexes) were maintained constant in all of these experiments, which causes the variation of the qualities of the resulting resonance peak (SI Figure S2). Since the performance of microcavities is mainly dependent on the cavity structure, it is expected that higher quality cavities can be obtained after further optimization of the cavity thickness.

Fabrication of AAO Microcavities (Type II) by Continuously Modifying the Phase of Effective Refractive Index in DBR Structure. The technique of inserting cavity layers is commonly used to fabricate high quality microcavities. A more challenging method is to utilize the phase difference of effective refractive index profiles of DBRs for achieving destructive interferences. Such protocol requires a precise control of the modulation of the effective refractive index profile perpendicular to the surface of the thin film, and the experimental realizations are rare in thin-film photonics technology.[28] To address this challenge, we engineered the anodization profile by introducing a phase change of pulse profile started at the 20th pulse cycle (SI Figure S3). Herein, we chose the condition of 140 s HVA as an example, in which the period of a single pulse was determined to be 1022.26 s (Figure 3e). Since the anodization profiles are translated into the effective refractive index of AAO, the phase of effective refractive index at the bottom DBR was shifted by programmed anodization profiles, resulting in the narrow resonance peak

DOI: 10.1021/acsami.5b01885
ACS Appl. Mater. Interfaces 2015, 7, 9879−9888

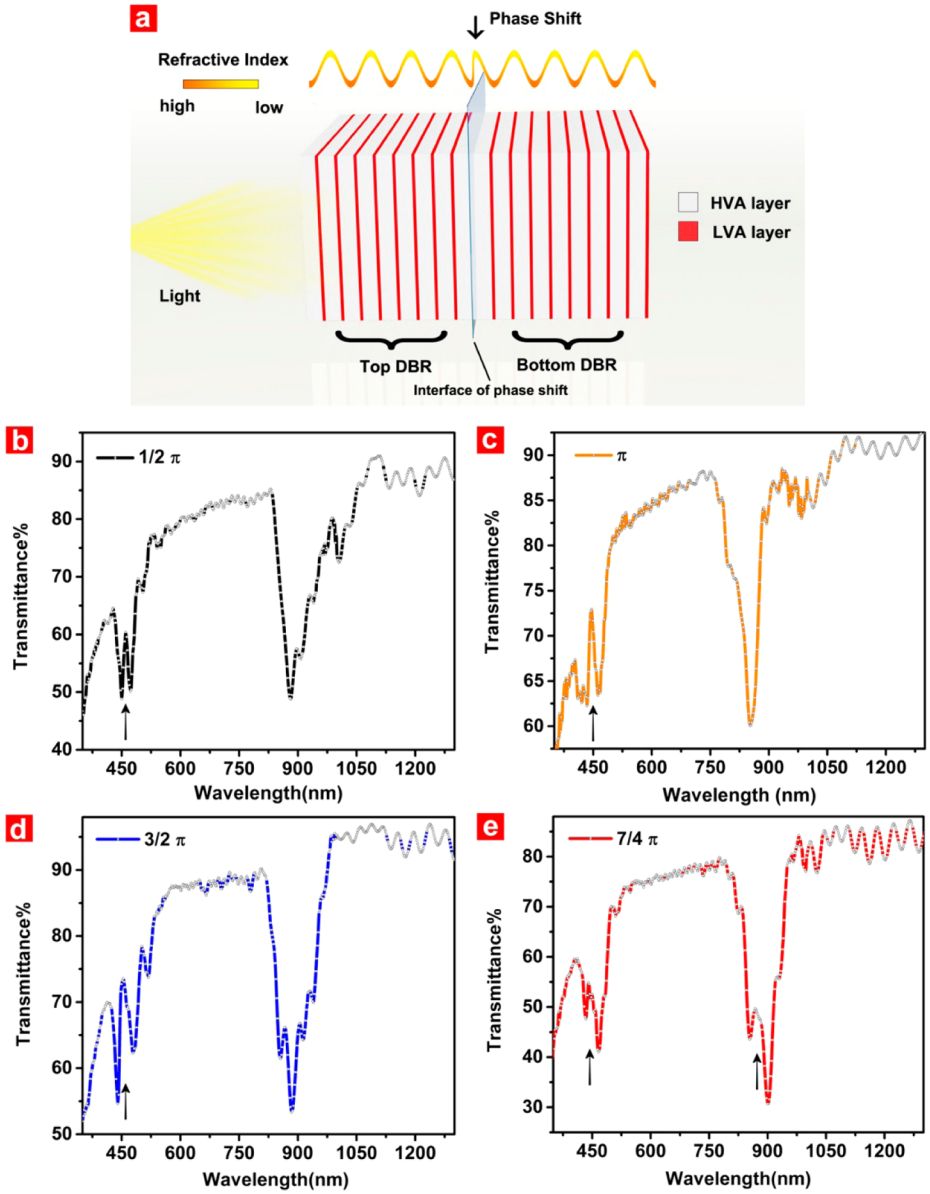

Figure 5. Phase shift of refractive index profile for preparation of AAO microcavities (type II). (a) Scheme of type II AAO microcavities prepared by continuous pulse anodization. The graded refractive index profile of the bottom DBR structure has a phase shift from 1/2 to 7/4 π to achieve the resonance with top DBR structure. (b–e) Transmittance profiles of AAO microcavities prepared by phase shift method. Black arrows denote the positions of resonance peaks.

within the stop band (Figure 5d–b). The second order resonance peak appeared with a 1/2 π phase shift and became stronger with a π phase shift due to the stronger destructive interferences between the upper and lower DBRs. In contrast, the first order resonance peak did not appear until the 7/4 π phase shift. From structural analysis, the modulation of pore geometry by 1/2 π phase shift is virtually undetectable by SEM characterization: straight pores were identified at the interface of the phase shift. However, branching of nanopores and variation of nanopore diameter appeared at the interface of the 7/4 π phase shift (SI Figure S4). We hypothesize that the absence of the first order resonance peak at 1/2 π–3/2 π phase shift is due to the delayed current recovery effect when anodization was switched from HVA to LVA. Although compromised by slowly reduced voltage to enable the continuous anodization at low voltage, the slow current recovery retarded the formation of nanopores at the beginning stage of LVA, thus delaying the translation of the phase profile into effective refractive index profile along the depth of AAO. It can be expected that anodization profiles aimed at facilitating the current recovery by increasing the electrolyte temperature and the use of sulfuric acid as electrolyte will efficiently address this limitation.[2,42]

Vapor Sensing Performance of AAO Microcavities. As a proof of applicability, we decided to demonstrate and asses the sensitivity of AAO microcavities toward water vapor. To this end, we exposed an AAO microcavity to a water vapor environment. It is known that the resonance peaks of microcavities structures are sensitive to changes in the refractive index of the medium inside the nanopores due to the photon confinement effect.[29,36] Since water vapor has higher refractive index than air, the accumulation of water molecules inside the nanopores will increase the effective refractive index of the AAO microcavity and thus will lead to a red shift of its

DOI: 10.1021/acsami.5b01885
ACS Appl. Mater. Interfaces 2015, 7, 9879–9888

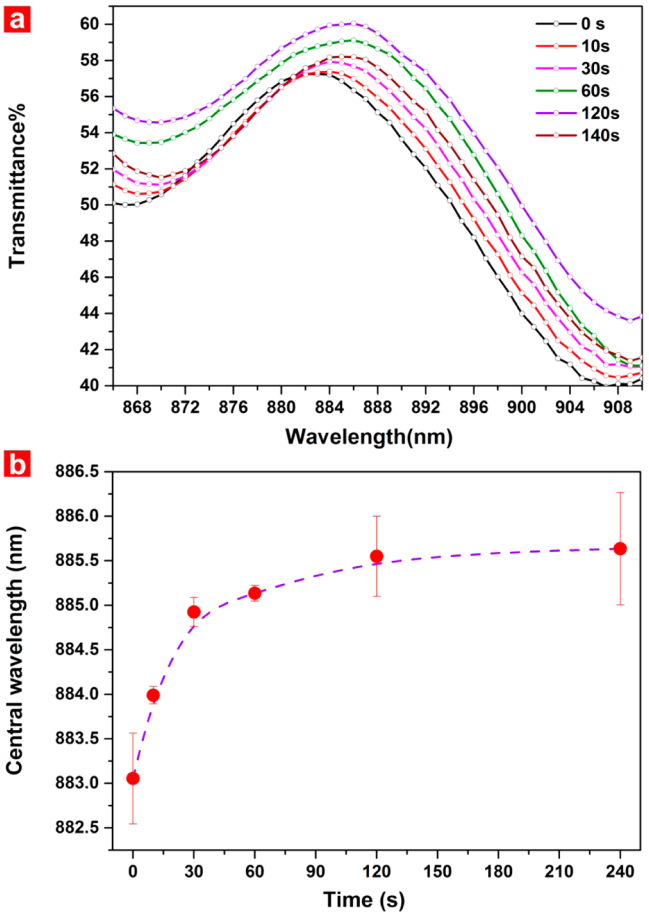

Figure 6. Water vapor sensing performance of AAO microcavities (type II) prepared with 7/4 π phase shift. (a) Transmittance profile of the resonance peak of AAO microcavities when exposed to water vapor at different time intervals. (b) Peak shift of the central wavelength against time after exposure to water vapor.

resonance peak. Transmittance spectra were recorded after vapor exposure at certain time points, and the shifts of the resonance peak were monitored as a function of time (Figure 6). We chose AAO microcavities (type II) with a 7/4 π phase shift as a sensor model. A red shift of the first order resonance peak appeared with a time-dependent fashion when the water vapor was condensed inside the nanopores of these AAO microcavities (Figure 6a). The resonance peak showed a central wavelength shift of 2.58 ± 0.37 nm in total after exposure to water vapor for 120 s, at which the saturation of the sensor was achieved. It is expected that AAO microcavities can be used for other gas sensing applications as well as biological/chemical sensing when combined with surface functionalization strategies.[25,44]

CONCLUSION

Although anodization of aluminum is a well-developed technique, the fabrication of advanced AAO-based photonic structures requires precise control over the nanoporous geometry for efficient light guiding. Herein, we have addressed this challenge by putting forward facile and rationally designed strategies for the fabrication of AAO microcavities by pulse anodization. Two types of AAO microcavities were synthesized by intercalating a cavity layer with constant refractive index between two AAO−DBR nanostructures and by programming phase shifts of effective refractive index profiles of AAO−DBR continuously along the depth of AAO. These methods not only enable a versatile tunability of the resonance peaks across the visible and near-infrared spectra but also open up new opportunities toward the design of more advanced AAO-based photonic nanostructures such as Thue−Morse, Fibonacci, and the combination of both, which potentially exhibit the novel patterns of resonance peaks and stop bands.[45] The resulting AAO microcavities presented in our study contained the features of Bragg stacks structures, making these structures easy to reproduce and exhibit good sensing potential. More importantly, these AAO optical structures when combined with other nanofabrication strategies such as atomic layer deposition and template replica offer solid foundations to prepare more sophisticated optical devices for a broad range of applications.[46]

ASSOCIATED CONTENT

Supporting Information

Further information about the branching structure characterization by SEM, transmission spectra of AAO microcavities (type I) prepared by different HVA durations, voltage and current density profiles, and the anodization profile/SEM images of AAO microcavities (type II). The Supporting Information is available free of charge on the ACS Publications website at DOI: 10.1021/acsami.5b01885.

AUTHOR INFORMATION

Corresponding Authors

*(A.S.) Tel.: +61 8 8313 1535. Fax: +61 8 8303 4373. E-mail: abel.santos@adelaide.edu.au. Web page: http://www.adelaide.edu.au/directory/abel.santos.

*(A.E.) Tel.: +618 8222 7451. Fax: +618 8222 7872. E-mail: andreas.evdokiou@adelaide.edu.au.

*(D.L.) Tel.: + 61 8 8313 4648 Fax: +61 8 8303 4373. E-mail: dusan.losic@adelaide.edu.au. Personal web page: http://www.adelaide.edu.au/directory/dusan.losic.

Author Contributions

Y.W. designed and conducted the experiments assisted by Y.C. The obtained results were discussed and analyzed by all of the authors. The final version of the manuscript was written through contributions of all the authors. All the authors have given approval to the final version of the manuscript.

Funding

This research was supported by the Australian Research Council (ARC) through Grants DE14010054 and FT110100711, the National Health and Medical Research Council (NHMRC) of Australia through Grant APP627015, the Australian Breast Cancer Research (ABCR), and the University of Adelaide Interdisciplinary Research Fund (DVC IRF-2014).

Notes

The authors declare no competing financial interest.

ACKNOWLEDGMENTS

We are thankful for Adelaide Microscopy for providing microscopy facilities. Y.W. appreciates the scholarship support from China Scholarship Council. This work was performed in part at the OptoFab node of the Australian National Fabrication Facility utilizing Commonwealth and SA State Government funding.

DOI: 10.1021/acsami.5b01885
ACS Appl. Mater. Interfaces 2015, 7, 9879−9888

ABBREVIATIONS

DBR, distributed Bragg reflectors
FWHM, full width at half-maximum
HVA, high voltage anodization
LVA, low voltage anodization
MA, mild anodization
RI, refractive index

REFERENCES

(1) Md Jani, A. M.; Losic, D.; Voelcker, N. H. Nanoporous anodic aluminium oxide: Advances in surface engineering and emerging applications. *Prog. Mater. Sci.* **2013**, *58* (5), 636−704.
(2) Lee, W.; Park, S.-J. Porous Anodic Aluminum Oxide: Anodization and Templated Synthesis of Functional Nanostructures. *Chem. Rev.* **2014**, *114* (15), 7487−7556.
(3) Losic, D.; Simovic, S. Self-ordered nanopore and nanotube platforms for drug delivery applications. *Expert Opin. Drug Delivery* **2009**, *6* (12), 1363−1381.
(4) Wang, Y.; Santos, A.; Kaur, G.; Evdokiou, A.; Losic, D. Structurally engineered anodic alumina nanotubes as nano-carriers for delivery of anticancer therapeutics. *Biomaterials* **2014**, *35* (21), 5517−5526.
(5) Santos, A.; Kumeria, T.; Losic, D. Nanoporous anodic aluminum oxide for chemical sensing and biosensors. *TrAC, Trends Anal. Chem.* **2013**, *44*, 25−38.
(6) Masuda, H.; Fukuda, K. Ordered Metal Nanohole Arrays Made by A 2-step Replication of Honeycomb Structures of Anodic Alumina. *Science* **1995**, *268* (5216), 1466−1468.
(7) Houser, J. E.; Hebert, K. R. The role of viscous flow of oxide in the growth of self-ordered porous anodic alumina films. *Nat. Mater.* **2009**, *8* (5), 415−420.
(8) Hebert, K. R.; Albu, S. P.; Paramasivam, I.; Schmuki, P. Morphological instability leading to formation of porous anodic oxide films. *Nat. Mater.* **2012**, *11* (2), 162−166.
(9) Nielsch, K.; Choi, J.; Schwirn, K.; Wehrspohn, R. B.; Gösele, U. Self-ordering Regimes of Porous Alumina: The 10 Porosity Rule. *Nano Lett.* **2002**, *2* (7), 677−680.
(10) Lee, W.; Kim, J.-C.; Gösele, U. Spontaneous Current Oscillations during Hard Anodization of Aluminum under Potentiostatic Conditions. *Advanc. Funct. Mater.* **2010**, *20* (1), 21−27.
(11) Thompson, G. E.; Wood, G. C. Porous anodic film formation on aluminium. *Nature* **1981**, *290* (5803), 230−232.
(12) Lee, W.; Ji, R.; Gosele, U.; Nielsch, K. Fast fabrication of long-range ordered porous alumina membranes by hard anodization. *Nat. Mater.* **2006**, *5* (9), 741−747.
(13) Yablonovitch, E. Photonic band-gap structures. *J. Opt. Soc. Am. B* **1993**, *10* (2), 283−295.
(14) Lee, W.; Schwirn, K.; Steinhart, M.; Pippel, E.; Scholz, R.; Gosele, U. Structural engineering of nanoporous anodic aluminium oxide by pulse anodization of aluminium. *Nat. Nanotechnol.* **2008**, *3* (4), 234−239.
(15) Lee, W.; Scholz, R.; Gösele, U. A Continuous Process for Structurally Well-Defined Al_2O_3 Nanotubes Based on Pulse Anodization of Aluminum. *Nano Lett.* **2008**, *8* (8), 2155−2160.
(16) Wang, Y.; Santos, A.; Evdokiou, A.; Losic, D. Rational Design of Ultra-Short Anodic Alumina Nanotubes by Short-Time Pulse Anodization. *Electrochim. Acta* **2015**, *154*, 379−386.
(17) Wang, K.; Liu, G.; Hoivik, N.; Johannessen, E.; Jakobsen, H. Electrochemical engineering of hollow nanoarchitectures: Pulse/step anodization (Si, Al, Ti) and their applications. *Chem. Soc. Rev.* **2014**, *43* (5), 1476−1500.
(18) Losic, D.; Lillo, M.; Losic, D., Jr. Porous Alumina with Shaped Pore Geometries and Complex Pore Architectures Fabricated by Cyclic Anodization. *Small* **2009**, *5* (12), 1392−1397.
(19) Zheng, W. J.; Fei, G. T.; Wang, B.; Jin, Z.; Zhang, L. D. Distributed Bragg reflector made of anodic alumina membrane. *Mater. Lett.* **2009**, *63* (8), 706−708.
(20) Biao, W.; Guang Tao, F.; Min, W.; Ming Guang, K.; De, Li Z., Preparation of photonic crystals made of air pores in anodic alumina. *Nanotechnology* **2007**, *18* (36), No. 365601.
(21) Rahman, M. M.; Marsal, L. F.; Pallarès, J.; Ferré-Borrull, J. Tuning the Photonic Stop Bands of Nanoporous Anodic Alumina-Based Distributed Bragg Reflectors by Pore Widening. *ACS Appl. Mater. Interfaces* **2013**, *5* (24), 13375−13381.
(22) Grzegorz, D. S.; Katarzyna, H. Distributed Bragg reflector based on porous anodic alumina fabricated by pulse anodization. *Nanotechnology* **2012**, *23* (7), No. 075303.
(23) Zheng, W.; Fei, G.; Wang, B.; De Zhang, L. Modulation of Transmission Spectra of Anodized Alumina Membrane Distributed Bragg Reflector by Controlling Anodization Temperature. *Nanoscale Res. Lett.* **2009**, *4* (7), 665−667.
(24) Guo, D.-L.; Fan, L.-X.; Wang, F.-H.; Huang, S.-Y.; Zou, X.-W. Porous Anodic Aluminum Oxide Bragg Stacks as Chemical Sensors. *J. Phys. Chem. C* **2008**, *112* (46), 17952−17956.
(25) Kumeria, T.; Santos, A.; Losic, D. Ultrasensitive Nanoporous Interferometric Sensor for Label-Free Detection of Gold(III) Ions. *ACS Appl. Mater. Interfaces* **2013**, *5* (22), 11783−11790.
(26) Chen, Y.; Santos, A.; Wang, Y.; Kumeria, T.; Wang, C.; Li, J.; Losic, D. Interferometric nanoporous anodic alumina photonic coatings for optical sensing. *Nanoscale* **2015**, DOI: 10.1039/C5NR00369E.
(27) Furchi, M.; Urich, A.; Pospischil, A.; Lilley, G.; Unterrainer, K.; Detz, H.; Klang, P.; Andrews, A. M.; Schrenk, W.; Strasser, G.; Mueller, T. Microcavity-Integrated Graphene Photodetector. *Nano Lett.* **2012**, *12* (6), 2773−2777.
(28) Hawkeye, M. M.; Brett, M. J. Narrow bandpass optical filters fabricated with one-dimensionally periodic inhomogeneous thin films. *J. Appl. Phys.* **2006**, *100* (4), No. 044322-1.
(29) Jenie, S. N. A.; Pace, S.; Sciacca, B.; Brooks, R. D.; Plush, S. E.; Voelcker, N. H. Lanthanide Luminescence Enhancements in Porous Silicon Resonant Microcavities. *ACS Appl. Mater. Interfaces* **2014**, *6* (15), 12012−12021.
(30) Böcking, T.; Kilian, K. A.; Reece, P. J.; Gaus, K.; Gal, M.; Gooding, J. J. Substrate Independent Assembly of Optical Structures Guided by Biomolecular Interactions. *ACS Appl. Mater. Interfaces* **2010**, *2* (11), 3270−3275.
(31) Kumeria, T.; Rahman, M. M.; Santos, A.; Ferré-Borrull, J.; Marsal, L. F.; Losic, D. Structural and Optical Nanoengineering of Nanoporous Anodic Alumina Rugate Filters for Real-Time and Label-Free Biosensing Applications. *Anal. Chem.* **2014**, *86* (3), 1837−1844.
(32) Auguié, B.; Fuertes, M. C.; Angelomé, P. C.; Abdala, N. L.; Soler Illia, G. J. A. A.; Fainstein, A. Tamm Plasmon Resonance in Mesoporous Multilayers: Toward a Sensing Application. *ACS Photonics* **2014**, *1* (9), 775−780.
(33) Brudieu, B.; Bris, A. L.; Teisseire, J.; Guillemot, F.; Dantelle, G.; Misra, S.; Cabarrocas, P. R. i.; Sorin, F.; Gacoin, T. Sol−Gel Route Toward Efficient and Robust Distributed Bragg Reflectors for Light Management Applications. *Adv. Opt. Mater.* **2014**, *2* (11), 1105−1112.
(34) Han, H.; Park, S.-J.; Jang, J. S.; Ryu, H.; Kim, K. J.; Baik, S.; Lee, W. In Situ Determination of the Pore Opening Point during Wet-Chemical Etching of the Barrier Layer of Porous Anodic Aluminum Oxide: Nonuniform Impurity Distribution in Anodic Oxide. *ACS Appl. Mater. Interfaces* **2013**, *5* (8), 3441−3448.
(35) Fang, C.-Y.; Liu, Y.-L.; Lee, Y.-C.; Chen, H.-L.; Wan, D.-H.; Yu, C.-C. Nanoparticle Stacks with Graded Refractive Indices Enhance the Omnidirectional Light Harvesting of Solar Cells and the Light Extraction of Light-Emitting Diodes. *Adv. Funct. Mater.* **2013**, *23* (11), 1412−1421.
(36) Jalkanen, T.; Mäkilä, E.; Suzuki, Y. I.; Urata, T.; Fukami, K.; Sakka, T.; Salonen, J.; Ogata, Y. H. Studies on Chemical Modification of Porous Silicon-Based Graded-Index Optical Microcavities for Improved Stability Under Alkaline Conditions. *Adv. Funct. Mater.* **2012**, *22* (18), 3890−3898.
(37) Yan, P.; Fei, G. T.; Shang, G. L.; Wu, B.; De Zhang, L. Fabrication of one-dimensional alumina photonic crystals with a

DOI: 10.1021/acsami.5b01885
ACS Appl. Mater. Interfaces 2015, 7, 9879−9888

narrow band gap and their application to high-sensitivity sensors. *J. Mater. Chem. C* **2013**, *1* (8), 1659−1664.
(38) Macias, G.; Ferré-Borrull, J.; Pallarès, J.; Marsal, L. 1-D nanoporous anodic alumina rugate filters by means of small current variations for real-time sensing applications. *Nanoscale Res. Lett.* **2014**, *9* (1), 1−6.
(39) Meng, G.; Jung, Y. J.; Cao, A.; Vajtai, R.; Ajayan, P. M. Controlled fabrication of hierarchically branched nanopores, nanotubes, and nanowires. *Proc. Natl. Acad. Sci. U. S. A.* **2005**, *102* (20), 7074−7078.
(40) Xing, H.; Zhiyuan, L.; Kai, W.; Yi, L. Fabrication of three dimensional interconnected porous carbons from branched anodic aluminum oxide template. *Electrochem. Commun.* **2011**, *13* (10), 1082−1085.
(41) Chen, B.; Xu, Q.; Zhao, X.; Zhu, X.; Kong, M.; Meng, G. Branched Silicon Nanotubes and Metal Nanowires via AAO-Template-Assistant Approach. *Adv. Funct. Mater.* **2010**, *20* (21), 3791−3796.
(42) Woo, L.; Jae-Cheon, K. Highly ordered porous alumina with tailor-made pore structures fabricated by pulse anodization. *Nanotechnology* **2010**, *21* (48), No. 485304.
(43) Su, Y.; Fei, G. T.; Zhang, Y.; Yan, P.; Li, H.; Shang, G. L.; Zhang, L. D. Controllable preparation of the ordered pore arrays anodic alumina with high-quality photonic band gaps. *Mater. Lett.* **2011**, *65* (17−18), 2693−2695.
(44) Kumeria, T.; Rahman, M. M.; Santos, A.; Ferré-Borrull, J.; Marsal, L. F.; Losic, D. Nanoporous Anodic Alumina Rugate Filters for Sensing of Ionic Mercury: Toward Environmental Point-of-Analysis Systems. *ACS Appl. Mater. Interfaces* **2014**, *6* (15), 12971−12978.
(45) Agarwal, V.; Miguel, E. M.-R. Optical characterization of polytype Fibonacci and Thue−Morse quasiregular dielectric structures made of porous silicon multilayers. *J. Phys. D: Appl. Phys.* **2007**, *40* (10), No. 3203.
(46) Martín, J.; Martín-González, M.; Francisco Fernández, J.; Caballero-Calero, O. Ordered three-dimensional interconnected nanoarchitectures in anodic porous alumina. *Nat. Commun.* **2014**, *5*, No. 5130.

DOI: 10.1021/acsami.5b01885
ACS Appl. Mater. Interfaces 2015, 7, 9879−9888